



Woodgate, M. A., Fitzgibbon, T. A. and Barakos, G. (2021) The Use of Computational Fluid Dynamics in the Investigation of Stall Onset on Tilt-Rotor Blades. In: 2021 AIAA AVIATION Forum, 2-6 Aug 2021, (doi:[10.2514/6.2021-2596](https://doi.org/10.2514/6.2021-2596))

The material cannot be used for any other purpose without further permission of the publisher and is for private use only.

There may be differences between this version and the published version. You are advised to consult the publisher's version if you wish to cite from it.

<http://eprints.gla.ac.uk/244839/>

Deposited on 25 June 2021

Enlighten – Research publications by members of the University of
Glasgow

<http://eprints.gla.ac.uk>

The Use of Computational Fluid Dynamics in the Investigation of Stall Onset on Tilt-Rotor Blades

Mark A. Woodgate*, T. A. Fitzgibbon† and George N. Barakos‡

School of Engineering, James Watt South Building, University of Glasgow, Glasgow, G12 8QQ, U.K.

An experimental setup has been designed to example the effect of tilt-rotor blade stall flutter. The blade has to be designed so that it does not exceed the maximum permissible load on the rotor rig to be employed for wind tunnel tests, while maximising the blade loading to allow for the blade to be excited. Computational fluid dynamics (CFD) has been used to design a set of blades to meet the requirements of an experimental rotor rig. After completion of the blade design the placement of the strain gauges for the experimental blade was achieved through the use of a three dimensional structural model. The modes of the blade were examined to allow placement of the strain gauges in regions of large expected strains.

I. Nomenclature

ALE	=	Arbitrary Lagrangian Eulerian
CAD	=	Computer Aided Design
CFD	=	Computational Fluid Dynamics
CSD	=	Computational Structural Dynamics
FEM	=	Finite Element Method
HMB3	=	Helicopter Multi-Block Solver
IDW	=	Inverse Distance Weighting
MENtOR	=	Methods and Experiments for NOvel Rotorcraft
UKVLN	=	UK Vertical Lift Network
SST	=	Shear Stress Transport (Menter)
URANS	=	Unsteady Reynolds Averaged Navier Stokes
C_p	=	pressure coefficient
c	=	Rotor chord
k	=	Number of nearest neighbours
R	=	Rotor radius
$R(W)$	=	Flux residual
V	=	Volume of a mesh cell
W	=	Vector of conserved flow variables

II. Introduction

MENtOR (Methods and Experiments for NOvel Rotorcraft) is a project of the UKVLN (UK Vertical Lift Network). The aim of MENtOR is to develop and validate methods and tools that can be used for the design and analysis of the next-generation rotorcraft. As part of this goal a comprehensive study of rotor blade flutter will be carried out using both simulations and experiments in the University of Glasgow de Havilland wind tunnel. CFD is used to support the experiment, find the stall flutter boundary and design blades that can stall while their loads are within the limits of the employed rotor testing facility.

Examples of propeller flutter include classical bending-torsion flutter which is govern by the interaction between the out-of-phase bending motion and the torsional motion are excited via an external aerodynamic loading[1] and stall flutter is defined as the oscillation of the body, due to partial or full separation of the flow field. Rotor blades are prone

*Research Associate, CFD Laboratory, Email: mark.woodgate@glasgow.ac.uk

†Research Assistant, CFD Laboratory, Email: t.fitzgibbon.1@research.gla.ac.uk

‡Professor, SMAIAA, MRaES, CFD Laboratory, Email: George.Barakos@glasgow.ac.uk

to working within the stall region due to the requirement of a large angle of attack on the retreating side of the rotor disk. A rotor blade experiencing a separated flow shows loading fluctuations which can alter the pitching moment acting on the blade which effects the blade pitch. The interaction of the non-linear aerodynamics and the blade structure produces a highly complex phenomena that cannot easily be modelled with low-fidelity methods. Hence methods that correctly capture the complex three-dimensional stalled flow and its interaction with the blade are required to accurately estimate the stall flutter boundary which will allow for improved blade design and expansion of the flight envelope [2].

III. Computational Methodology: HMB3

For the investigation into rotor blade stall flutter, a time-marching aeroelastic method has been used. This method involves the coupling between Computational Fluid Dynamic (CFD) and Computational Structural Dynamics (CSD).

A. Computation Fluid Dynamics

All calculations were performed using the parallel CFD solver HMB3 (Helicopter Multi Block) [3]. HMB3 has previous been used several propeller flow comparisons with the experimental data. These include the results of the JORP blade [4] and the IMPACTA wind tunnel test [5].

HMB3 solves the dimensionless 3D Navier-Stokes equations in integral form using the Arbitrary Lagrangian Eulerian (ALE) formulation [6] for time-dependent domains with moving boundaries. The unsteady Reynolds-averaged Navier-Stokes equation are discretised using a cell-centred finite volume approach on a multi-block grid. A curvilinear coordinate system is adopted to simplify the formulation of the discretized terms, since body-conforming grids are adopted.

The spatial discretisation of these equations leads to a set of ordinary differential equations in time,

$$\frac{d}{dt} [WV] + R(W) = 0. \quad (1)$$

In the above W is the vector of conserved variables, V denotes the volume of the cell and $R(W)$ represents the flux residual. Using a fully implicit time discretisation and approximating the time derivative by a second order backward difference equation (1) becomes

$$\frac{3V^{n+1}W^{n+1} - 4V^nW^n + V^{n-1}W^{n-1}}{2\Delta t} + R(W^{n+1}) = 0. \quad (2)$$

This equation is defined to be the unsteady residual R^* . Following the original implicit dual-time approach introduced by Jameson [7] equation (2) is solved by iteration in pseudo-time t^* . Using an implicit time discretisation on the pseudo-time t^* we can write

$$\frac{W^{m+1} - W^m}{\Delta t^*} = -\frac{R^*(W^{m+1})}{V} \quad (3)$$

where the superscript $m + 1$ denotes the time level $(m + 1)\Delta t^*$ in pseudo-time. The unsteady flux residual $R^*(W^{m+1})$ is linearised in the pseudo-time variable t^* to form the sub iteration for solving equation 2 at each real t time step.

Osher's upwind scheme [8] is used to resolve the convective fluxes for its robustness, accuracy and stability properties. The Monotone Upstream-centered Schemes for Conservation Laws (MUSCL) [9] variable extrapolation method is employed in conjunction to formally provide second-order accuracy. The van Albada limiter [10] is also applied to remove any spurious oscillations across shock waves. The linear system is solved using a Krylov subspace algorithm, the generalized conjugate gradient method, with a block incomplete lower-upper (BILU) factorization as a pre-conditioner. The viscous stress tensor is approximated in HMB3 using the Boussinesq hypothesis. The two-equation turbulence model of $k-\omega$ has been implemented into flow solver [11].

HMB3 uses overset grids [12] to allow for the relative motion between different mesh components. For the present work, overset grids are employed to ease the generation and deformation of the rotor blades, and to allow for the relative motion for the rotor with respect to the rotor rig and the wind tunnel walls.

B. Computational Structural Dynamics

There are a number of aero-elastic formulations in HMB3 and this work uses a "middleware" to directly couple HMB3 to MSC/NASTRAN. The middleware is the interface between HMB3D and MSC/NASTRAN and is responsible for the

interpolation of the Oreo dynamic loading between the CFD blade surface mesh and the points when the loads are applied on the structural model and the interpolation of the displacements from MSC/NASTRAN to the CFD blade surface mesh. The surface interpolation is performed with the Moving Least Square method (MLS). This method is accurate as loads integration's and displacement computations are carried out on the CFD grid with out interpolation while the CFD volume mesh, within the body fitted chimera mesh only, uses Inverse Distance Weighting (IDW). IDW is a multivariate interpolation method that calculates the value at an unknown point with a weighted average of the values of a known set of scattered points. The weight assigned to the value at a known point is proportional to the inverse of the distance between the known and the unknown point (see Shepard [13]). HMB3 uses the a modified Shepard's method, which was proposed by Renka [14] and calculates the interpolated value using only the k nearest neighbours within the R -sphere (k and R are given fixed parameters) instead of all the points.

The robustness of the volume mesh displacements is greatly improved by splitting the displacement into two parts the mean displacement plus optimal solid body rotation and the remainder. The mean displacement plus optimal solid body rotation can be applied exactly to the body fitted chimera mesh while the remainder, which is generally much smaller than the original displacements, use the inverse distance weighting (IDW) interpolation method.

IV. Rotor Rig

The rotor rig is to be installed at the university of Glasgow de Havilland wind tunnel which is part of the UK national wind tunnel facility and is shown in figure 1. It is a closed return tunnel with an octagonal working cross section 2.66m wide by 2.1m high and 5.4m long with a maximum speed of 70m/s. The power limits of the rotor rig are shown in table 1.

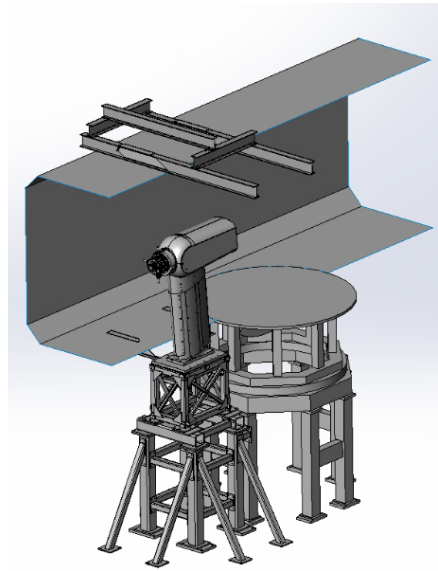


Fig. 1 Cutaway section of the Glasgow de Havilland wind tunnel and rotor rig.

	Thrust	Torque	Power	Diameter
Maximum	3.4kW	350Nm	80kW	< 1.5m

Table 1 Thrust, torque and power limits for the rotor rig.

V. Blade Design

The dimensions of the blade are shown in table 2. The blade shape was obtained by using a second order polynomial to blend between sections. The blade sections were modified around the leading edges through the addition and smoothing of the control points and the trailing edge thickness was increased.

Parameter		Parameter		Section	Name
Rotor radius	625mm	Cone angle	0°	Y=190mm	NACA 64-128
Root chord	84.2mm	Tip chord	60.0mm	Y=360mm	Vertol V43015_2.48
Inboard cut-off	186mm	Trailing Edge thickness	0.47mm	Y=615mm	Vertol V23010_1.58

Table 2 Characteristics and dimensions of the model rotor blade design.

A. Structural Components

The aerofoil skin was made from composite material of carbon epoxy resin and was approximately 1mm thick. To increase the stiffness of the aerofoil skin a composite D spar with a foam core was included. The root fitting was manufactured from aluminium to keep the weight down. Since the blades are removable a shear pin manufactured from maraging steel is used to connect the blades to the pitch shaft. To increase the root fitting in the area around the shear pin, collar rings of maraging steel were also included. Finally, the root tip is used as a balancing solution. The blades structure can be seen in figure 2 as well as the structural mesh for components.

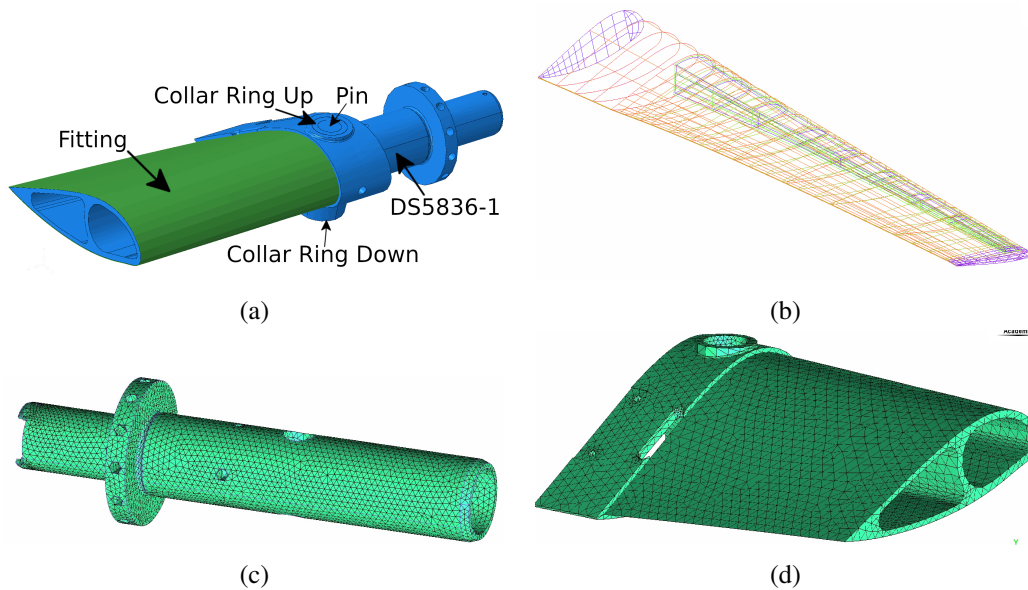


Fig. 2 Blade structure: (a) Fitting and components connecting the blade to the hub, (b) Surface skin, D spar and tip cap, (c) structural mesh for the DS5836-1, (d) structural mesh for the fitting.

B. MSC/NASTRAN Model

The full CAD model was used in the construction of the unstructured finite element mesh. Each component was generated separately using a mixture of tetrahedra, pyramids, prisms and hexahedra which all have their corresponding 3D solid elements within MSC/NASTRAN (CTETRA,CPYRAM,CPENTA,CHEXA). The volume mesh sizes are presented in table 3. As can be seen from the ratio of hexahedra to total elements the blade skin, D spar and foam fillers, used predominantly hexahedra elements while the more complex shaped components used only tetrahedra. The components were connected via two different methods. The surfaces that co-inside on the skin, D spar and foam fillers are exactly the same and are connected by merging the nodes on these surfaces to construct the volume mesh with a set of unique mesh points. However this is not possible to achieve this with the triangular surface mesh associated with the fitting and the quadrilateral mesh associated with blade skin. These components are connected through MSC/NASTRAN support of permanent glued contact. It should be noted that the two surfaces do not have to co-inside as the permanent glued contact used allows for maintaining an initial gap or an overlap between the nodes of the glued bodies. The segment-to-segment contact region was used because it tends to produce a more continuous distribution of stresses across the discontinuous glued interface compared to the the node-to-segment method [15].

Each component is added to a three dimensional deformable contact body using BCBODY1 and these are connected together through the definition of a contact pair (BCONNECT) which have geometric and physical contact parameters which describe the type of contact involved. Then, each pair is added to a contact table (BCTABL1). Single point constraints were also used on the root of the fitting to clamp the root of the blade for modal analysis.[15, 16]

VI. Computational Setup and MSC/NASTRAN Analysis

A blade spinning at 3000 RPM results in a tip speed of 196m/s with an inflow velocity set at 38m/s which equates to 0.194 of the tip velocity. This inflow velocity is relatively small compared to the tip velocity but is at the upper limit of what the wind tunnels can deliver. These conditions result in a tip Reynolds number of 0.854 million.

Figure 3 shows the surface pressure coefficient at six different collectives. A recirculation bubble starts to form when the collective reaches 31° . By the time the collective is at 34° the flow has a very large recirculation region.

Figure 4 shows the cross-section pressure coefficient through the recirculation bubble, scaled with the local wind velocity, at 88.4% and 93.4% span for a range of collective values. At both stations, as the collective increases the suction peak strengthens and stall occurs, signified by the pressure coefficient at the trailing edge decreasing causing a fairly constant pressure coefficient over the final 70% of the chord. This effect occurs at 32° collective at the inboard station and a degree later at the outboard station as the separation bubble expands in the spanwise direction. This indicates that the onset of stall is around the 32° collective.

Table 5 shows the different thrust, torque and power requirements for the different collective values. At 32° degrees of collective both the thrust and torque are well within their specs of the rotor rig while the power requirements are high. This will be okay in practise since the motor on the rotor rig is rated at 140kW and a deliverable power of 80kW is conservative for a direct drive system when taking losses into account.

Finally, figure 5 shows the start of the separation bubble at 31° collective, and an expanded bubble at 33° collective, as well as, a well defined tip vortex. There is a large recirculating flow region on the upper surface of the blade signifying the blade is likely to have already stalled.

Table 4 presents the non rotational modal shapes and frequencies calculated using the full FEM model. It was found that the inclusion of the effect of the blade rotation, which has a stiffening effect on the blade, only increased the frequencies by a couple of percent which is typically less than the blade to blade variation due to the manufacturing process. Figure 6 shows the displacement of the first bending and torsion modes.

The strain gauges need to be placed to monitor the bending and torsional loads. The idea is to try and minimise the number of gauges to monitor and need to be placed in region of the blade which undergo the largest stretching, or compression of the blade for each mode. Figure 7 shows the placement on the strain gauges on the upper and lower composite surface.

VII. Conclusions and future work

The newly designed blade has a torque at the onset of stall about 285Nm and within specification of the rotor rig to be employed for tests. This is likely to be an over-estimate since finer grids calculations normally reduce both the thrust and torque of the blade from a CFD simulation. Also the calculations used the Reynolds averaged Navier stokes (RANS) and Menter's shear stress transport turbulence model that also delays the onset of stall compared to a more realistic unsteady SST-SAS (Menter's shear stress transport with scale-adaptive simulation) turbulence model. This model uses unsteady Reynolds average Navier-Stokes (URANS) with large eddy simulation (LES) type content in the unsteady regions and produces less eddy viscosity away from the solid walls.

A 3D finite element was built using the CAD model of the blade and normal mode analysis was used to find the regions undergoing the largest stretching, or compression for each mode. These regions are where the strain gauges have been placed.

Future work includes running coupled aeroelastic calculations, with the wind tunnel modelled to examine the blockage effects, and dynamic simulations to examine the behaviour of the blade as it spins up and transition to the correct conditions without damaging the blade or the rotor rig stops. The blade is currently under construction and test results will be used to validate the computer simulations after the experimental campaign.

Acknowledgments

This work is funded by MENtOR (EP/S013814/1). The work also used the Research Computing for the West of Scotland service ARCHIE-WeSt (<http://www.archie-west.ac.uk>) the Cirrus UK National Tier-2 HPC Service at EPCC (<http://www.cirrus.ac.uk>) under project ec004 and the ARCHER2 UK National Supercomputing Service (<http://www.archer2.ac.uk>) under project e613.

References

- [1] Wright, J. R., and Cooper, J. E., *Introduction to aircraft aeroelasticity and loads*, 2nd ed., John Wiley & Sons, 2015.
- [2] Higgins, R. J., Jimenez-Garcia, A., Barakos, G. N., and Bown, N., “High-fidelity computational fluid dynamics methods for the simulation of propeller stall flutter,” *AIAA Journal*, Vol. 57, No. 12, 2019, pp. 5281–5292.
- [3] Stejtl, R., Barakos, G., and Badcock, K., “A framework for CFD analysis of helicopter rotors in hover and forward flight,” *International Journal for Numerical Methods in Fluids*, Vol. 51, No. 8, 2006, pp. 819–847.
- [4] Scrase, N., and Maina, M., “The evaluation of propeller aero-acoustic design methods by means of scaled-model testing employing pressure tapped blades and spinner,” *ICAS PROCEEDINGS*, Vol. 19, AIAA, 1994.
- [5] Gomariz-Sancha, A., Maina, M., and Peace, A. J., “Analysis of propeller-airframe interaction effects through a combined numerical simulation and wind-tunnel testing approach,” *53rd AIAA Aerospace Sciences Meeting*, Kissimmee, Florida, 2015. AIAA 2015-1026.
- [6] Hirt, C., Amsden, A., and Cook, J., “An arbitrary Lagrangian-Eulerian computing method for all flow speeds,” *Journal of Computational Physics*, Vol. 14, No. 3, 1974, pp. 227 – 253.
- [7] Jameson, A., “Time Dependent Calculations Using Multigrid, with Applications to Unsteady Flows Past Airfoils and Wings,” *10th Computational Fluid Dynamics Conference*, Honolulu, HI, 1991. AIAA-1991-1596.
- [8] Osher, S., and Chakravarthy, S., “Upwind schemes and boundary conditions with applications to Euler equations in general geometries,” *Journal of Computational Physics*, Vol. 50, No. 3, 1983, pp. 447–481.
- [9] van Leer, B., “Towards the ultimate conservative difference scheme. V. A second-order sequel to Godunov’s method,” *Journal of Computational Physics*, Vol. 32, No. 1, 1979, pp. 101–136.
- [10] Van Albada, G., Van Leer, B., and Roberts Jr, W., “A comparative study of computational methods in cosmic gas dynamics,” *Astronomy and Astrophysics*, Vol. 108, 1982, pp. 76–84.
- [11] Menter, F., “Two-Equation Eddy-Viscosity Turbulence Models for Engineering Applications,” *AIAA Journal*, Vol. 32, No. 8, 1993, pp. 1598–1605.
- [12] Jarkowski, M., Woodgate, M., Barakos, G. N., and Rokicki, J., “Towards consistent hybrid overset mesh methods for rotorcraft CFD,” *International Journal for Numerical Methods in Fluids*, Vol. 74, No. 8, 2014, pp. 543–576.
- [13] Shepard, D., “A Two-dimensional Interpolation Function for Irregularly-spaced Data,” *Proceedings of the 1968 23rd ACM National Conference*, Assoc. for Computing Machinery, New York, NY, USA, 1968, pp. 517–524.
- [14] Renka, R. J., “Multivariate Interpolation of Large Sets of Scattered Data,” *ACM Trans. Math. Softw.*, Vol. 14, No. 2, 1988, pp. 139–148.
- [15] *MSC Nastran 2021 Nonlinear (SOL 400) User’s Guide*, MSC Software Corporation, 2020.
- [16] *MSC Nastran 2021 SOL 400 Getting Started Guide*, MSC Software Corporation, 2020.

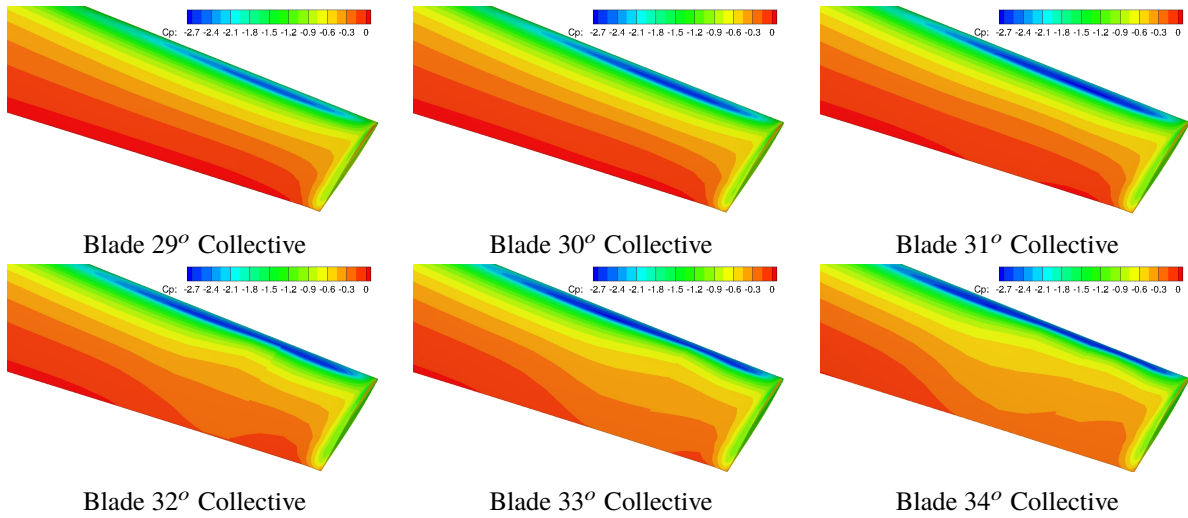


Fig. 3 Pressure coefficient for the rotor blade spinning at 3000 RPM with an inflow velocity 38m/s and tip Reynolds number of 0.864 million at six different collectives angles.

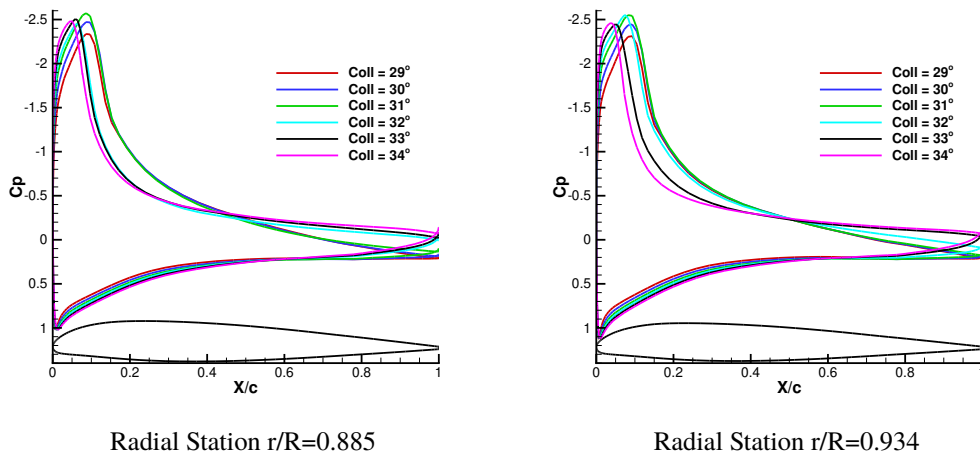


Fig. 4 Comparison of sectional pressure coefficient at two different stations along the blade at different collective settings.

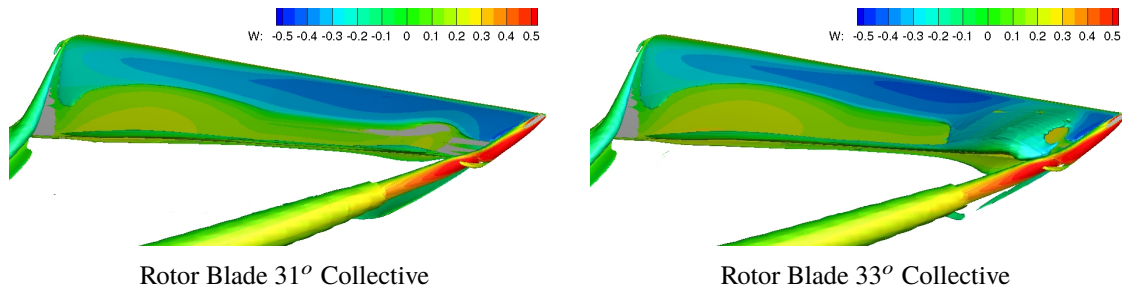


Fig. 5 Size of the separation bubble for the blade spinning at 3000 RPM at an inflow velocity of 38m/s and tip Reynolds number of 0.864 million.

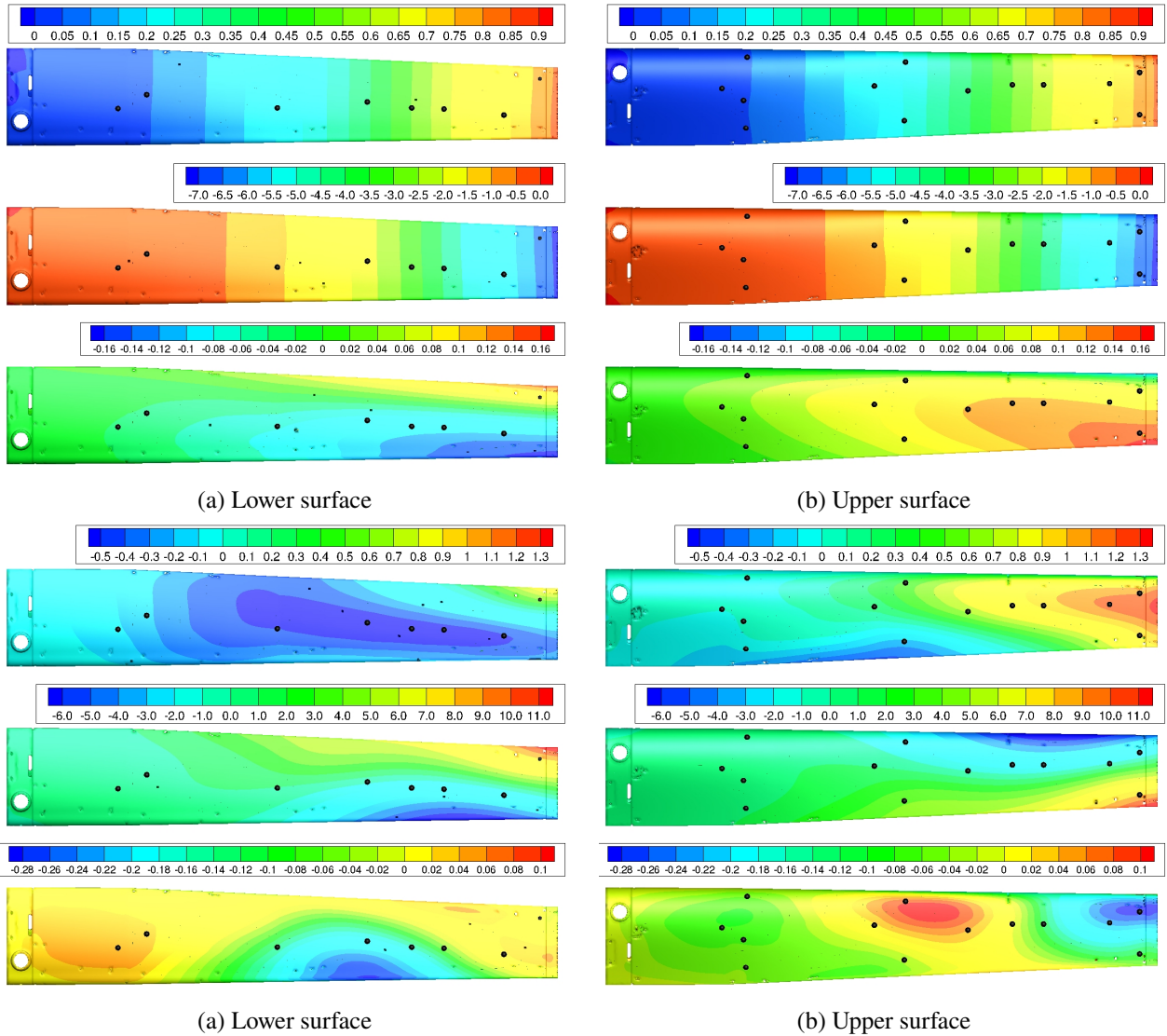
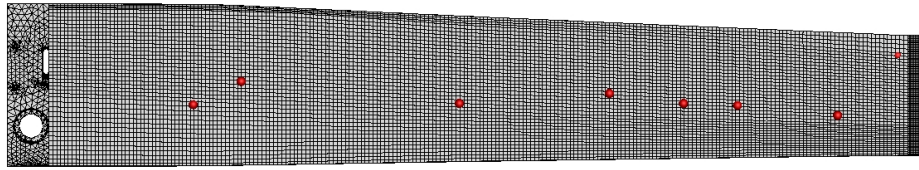


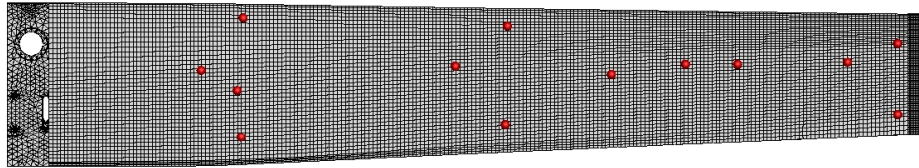
Fig. 6 The displacement of the first bending and first torsion modes of the blade design.

Part	No. Nodes	No. Elements	No. Tetra	No. Pyramids	No. Prisms	No. Hexa
Root Fitting	9102	35522	35522	0	0	0
Pin	41615	195392	195392	0	0	0
Up Collar Pin	1341	1106	88	127	117	774
Down Collar Pin	2215	1852	98	180	206	1368
Blade Skin	37682	19696	138	413	886	18259
Beam	14360	8396	218	645	1085	6448
Beam Core	15814	14517	717	2081	879	10840
Rear Filler	20285	17146	615	1677	809	14045
Tip Cap	12174	13350	2606	4682	788	5274
Total	154588	306977	235394	9805	4770	57008

Table 3 Rotor blade structural grid properties



(a) Lower surface



(b) Upper surface

Fig. 7 Placement of the strain gauges

Number	Shape	Frequency (Hz)
1	Flapwise bending	88.3
2	Lag Bending	288.9
3	Flapwise bending + Lag Bending	393.0
4	Flapwise bending	704.9
5	Torsion	756.5
6	Flapwise bending	1118.5

Table 4 Rotor blade normal modes.

Collective Angle	Rotor Blade		
	Thrust N	Torque Nm	Power (kW)
25.0°	737	149	46.8
27.0°	1119	199	62.4
29.0°	1277	236	73.9
30.0°	1345	253	79.5
31.0°	1401	270	84.7
32.0°	1426	285	89.3
33.0°	1453	299	93.8
34.0°	1468	313	98.1
35.0°	1486	328	102.9
36.0°	1499	344	108.1

Table 5 Total thrust torque and power for the blade at different collective settings